Simultaneous Closed-Loop Local Calibration of Robot and Extrinsic Parameters of Robot-Mounted Measurement Devices

Mohammadreza Dehghani*, Ryan A. McKenzie, Rishad A. Irani, Mojtaba Ahmadi

Department of Mechanical and Aerospace Engineering at Carleton University, Ottawa, Ontario, K1S 5B6, Canada

Abstract

This paper presents a method for simultaneously calibrating the kinematic parameters of robot and robot-mounted measurement devices. The Modified Denavit-Hartenberg parameters are extended to include the world and tool frames within a minimal parameter set using a systematic approach. Closed-loop calibration is performed using the data collected in the local target workspace using the robot-mounted measurement device. The presented modeling and calibration methods are applied to a case study in which a machining task is performed using a DENSO VS-6556W industrial robot equipped with a cutting tool, force sensor, and laser profile scanner. In the case study, local models are calibrated for the laser and tool frames using common 1-2-3 blocks as calibration artifacts. The robot/laser model is identified by scanning the artifacts with a robot-mounted laser scanner, and the robot/tool model is calibrated by touching the artifacts with a robot-mounted force sensor. In this application, the robot/laser model is used to scan and register a sheet metal workpiece, and the robot/tool model is used to plan a tool path to machine the periphery. Positional accuracy of the tool path was evaluated to be ± 0.15 mm within the target workspace, which shows significant improvement compared with the mean error of 0.8 mm achieved by global calibration of the robot/tool model.

Keywords: Kinematics, Calibration and Identification, Local Calibration, Industrial Robots.

*Corresponding author

Email addresses: Reza.Dehghanitafti@carleton.ca (Mohammadreza Dehghani), RyanA.McKenzie@carleton.ca (Ryan A. McKenzie), Rishad.Irani@carleton.ca (Rishad A. Irani), Mojtaba.Ahmadi@carleton.ca (Mojtaba Ahmadi)

1. Introduction

Industrial robots are widely used to automate tasks that require high repeatability, speed, and flexibility. Despite many advantages, industrial robots have relatively low accuracy. For manufacturing tasks that require higher accuracy, manual methods are still prevalent and represent a large portion of manufacturing costs [1]. For example, typical aerospace parts include small radii, holes, slots and scallops with break sharp edge requirements in the range of 0.1 mm to 1 mm [2], which may be difficult to achieve with a robotic solution. There is extensive demand for robotic solutions to reduce cost, improve processing time, and mitigate safety hazards in industrial environments. For these high-accuracy applications, further investigation is required to improve accuracy through parametric modeling and calibration.

Kinematic calibration of industrial robots is a well-developed area that consists of four steps: modeling, measurement, identification, and compensation [3]. The modeling step provides a mathematical model that defines the end-effector pose based on the robot parameters and joint variables. The measurement step includes moving the robot through a series of poses and collecting the joint angles along with the end-effector pose. In the identification step, an optimization algorithm minimizes the error between the measured poses and poses that are estimated using the robot model. In the compensation step, the identified parameters are applied to the robot model used in path planning and control, reducing the pose errors and thereby increasing accuracy.

Calibration methods are generally categorized into open-loop and closed-loop methods [4]. The open-loop approach is performed by measuring the pose of the end-effector through an external measurement device, such as a coordinate measuring machine (CMM) [5], measurement arm [6], stereo-vision system [7], optical CMM [8], or laser tracker [8, 9, 10, 11]. One approach to closed-loop calibration is to constrain the end-effector motion and record the joint angles in different poses. Applying the constraints to the model results in a set of equations that could be used in parameter identification. A variety of constraints have been proposed, including point [12, 13, 14], point and distance [15], planar [16, 17], cylindrical [18], and spherical constraints [19]. A similar approach is to collect measurements from known artifacts. Goswami et al. measure the end-effector distance from a fixed location using a linear variable distance transducer (LVDT) [20]. Joubair et al. probed three spheres with known center-to-center distances [19]. Measurements could be collected by contact sensors, such as touch probes, or by non-contact sensors attached to the end-effector [21].

While uncalibrated robots typically exhibit positional errors between 5 mm to 15 mm, calibrated robots often have errors around 1 mm [22]. Including non-geometrical parameters such as joint flexibility in the model can further improve the accuracy of calibration to submillimeter range [9]. Global calibrations are typically performed by collecting measurement data throughout the workspace and identifying a global parameter set that minimizes error for all measurements. This global method yields optimal average error over the whole workspace; however, local positioning errors may be much larger at specific points or subareas.

Consequently, model accuracy may be lower than expected in some regions of the workspace. Research on error compensation showed that robot models exhibit positional error similarity [23, 24]. In addition, Nubiola et al. [9] showed that restricting the calibration to a subarea defined by a 0.7 m cube reduced the mean positional error from 0.364 mm to 0.292 mm. Therefore, it is expected that a local calibration for a subarea of the workspace will have higher accuracy than a global calibration [25], which is well-suited for applications where a smaller, more accurate workspace is required.

The contribution of this work is a method for simultaneously calibrating robot and tool/sensor frame parameters using robot-mounted measurement devices. The proposed method is flexible in selection of calibration artifact and its placement, making the selection of a desired local target workspace possible. This method is specifically advantageous in manufacturing applications where target workspace of the robot is restricted based on workpiece size and clamping options. As the kinematic model is calibrated for a local area, it can be more accurate than the global calibration when operating within the target area. The use of robot-mounted measurement devices results in a straightforward and repeatable measurement process for a local target workspace.

Additionally, the current work provides a systematic method to include the world and tool frames in Modified Denavit-Hartenberg (MDH) parameters [26] while ensuring a minimal set of model parameters. The systematic assignment of frames prevents model singularities, and it is useful for practitioners and researchers in the field of robotics.

An additional advantage of the proposed method is the ability to calibrate the entire model without removing the end-effector. Many common methods require removal of the end-effector so that specialized sensory equipment may be attached during the calibration process. The end-effector may be reattached afterwards; however, a change of components after calibration, such as changing the tool and/or moving fixtures, may result in inaccuracies in the final process. Utilizing the extended model, as discussed herein, has the advantage that the world and tool frames will be calibrated along with the robot parameters, which is critical for achieving high accuracy. Simultaneous calibration of all parameters ensures that no further error is introduced due to moving the tool/sensor after calibration.

To demonstrate industrial application, the proposed method is applied to a case study in which a machining operation is performed by a robot equipped with a cutting tool and laser profile scanner. The calibration artifacts are standard 1-2-3 blocks, which are commonly used in machining operations.

In Section 2, the systematic approach for extending the robot model to include world and tool frames is presented, and the identification process for local calibration of the extended model is discussed. In Section 3, the model is applied to an industrial robot equipped with a cutting tool and a laser profile scanner. The two kinematic chains are calibrated using a common calibration artifact. Achievable positional accuracy is verified through experimental results presented in Section 4 and conclusions are stated in Section 5.

2. Calibration Methodologies

The first step in the proposed calibration process is to define a kinematic model. In practice, the world and tool frames must be included in the model for calibration.

The key concept of the proposed local calibration is to use robot-mounted measurement devices to interact with a simple calibration artifact in the target workspace. The interaction may be through physical contact or measurements using a non-contact sensor. The joint positions when the robot interacts with the artifact in different poses and the known dimensions of the artifact are used for parameter identification. The calibration artifact can be moved or reconfigured to create more constraints to improve the calibration; nevertheless, the constraints should remain within the target workspace.

Based on the application, various tools and sensors may be mounted on the robot end-effector. In the measurement step, a set of robot poses must be defined to interact with the calibration artifact. For machine tools, a path is generated to create contact between the tool and the artifact. The contact could be detected with force sensors, touch probes, or a reliable continuity test. For non-contact sensors, a path is generated to move the robot to desired poses and record measurements of the calibration artifact. Robot joint positions along with the sensor measurements are used for calibration.

2.1. Robot Modeling

The kinematic model of a serial manipulator is commonly formulated using the Denavit-Hartenberg (DH) approach [27]. The base frame (0) is assigned to the robot base, and subsequent frames (1 to n) are attached to each link.

Fig. 1 illustrates the geometric parameters of a link, which describe the relationship between two neighboring frames. The DH approach uses four independent parameters, namely joint angle θ_i, link offset d_i, link length a_i, and

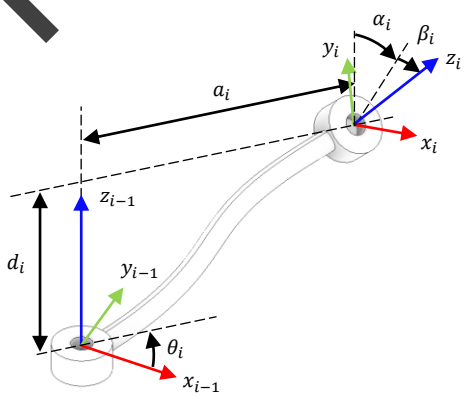

Figure 1: The joint angle θ_i, the link offset d_i, the link length, a_i, the link twist, α_i, and the additional parameter β_i describe the transformation between neighboring links.

link twist α_i. Using these DH parameters, the pose of frame i with respect to frame $(i-1)$ is written as a transformation matrix,

$$ {}^{i-1}\mathbf{H}_i(\theta_i) = \mathrm{Rot}_{z,\theta_i}\mathrm{Trans}_{z,d_i}\mathrm{Trans}_{x,a_i}\mathrm{Rot}_{x,\alpha_i}\,. \tag{1} $$

A number of researchers have determined the limitations of DH approach and proposed modifications for the modeling procedure [3]. Specifically for calibration applications, If two consecutive frames have near-parallel z-axes, the geometric model is poorly defined. Hayati [26] introduced an extra rotation parameter β_i about the y-axis for this case. The DH parameters and the additional y-axis rotation parameter are collectively the so-called Modified Denavit-Hartenberg (MDH) parameters. Using the MDH parameters, the transformation from frame $(i-1)$ to frame i is

$$ {}^{i-1}\mathbf{H}_i(\theta_i) = \mathrm{Rot}_{z,\theta_i}\mathrm{Trans}_{z,d_i}\mathrm{Trans}_{x,a_i}\mathrm{Rot}_{x,\alpha_i}\mathrm{Rot}_{y,\beta_i} \tag{2} $$

where the matrix/vector components are defined as

$$ {}^{i-1}\mathbf{H}_i(\theta_i) = \left[\begin{array}{c|c} {}^{i-1}\mathbf{R}_i & {}^{i-1}\mathbf{d}_i \\ \hline \mathbf{0} & 1 \end{array}\right], $$

$$ {}^{i-1}\mathbf{R}_i = \begin{bmatrix} c_{\beta_i}c_{\theta_i} - s_{\alpha_i}s_{\beta_i}s_{\theta_i} & -c_{\alpha_i}s_{\theta_i} & s_{\beta_i}c_{\theta_i} + c_{\beta_i}s_{\alpha_i}s_{\theta_i} \\ c_{\beta_i}s_{\theta_i} + s_{\alpha_i}s_{\beta_i}c_{\theta_i} & c_{\alpha_i}c_{\theta_i} & s_{\beta_i}s_{\theta_i} - c_{\beta_i}s_{\alpha_i}c_{\theta_i} \\ -c_{\alpha_i}s_{\beta_i} & s_{\alpha_i} & c_{\alpha_i}c_{\beta_i} \end{bmatrix}, $$

$$ {}^{i-1}\mathbf{d}_i = \begin{bmatrix} a_i c_{\theta_i} & a_i s_{\theta_i} & d_i \end{bmatrix}^{\mathrm{T}}, $$

where the notation c_ϕ and s_ϕ are used to represent $\cos(\phi)$ and $\sin(\phi)$, respectively.

For each joint in the kinematic chain, either d_i or β_i is set to zero. If joints i and $(i+1)$ are near-parallel, d_i is set to zero; otherwise, β_i is zero. Thus, a set of four independent parameters may be selected for each assigned frame. The overall transformation of an n-DOF robot kinematic chain is

$$ {}^{0}\mathbf{H}_n(\boldsymbol{\theta}) = \prod_{i=1}^{n} {}^{i-1}\mathbf{H}_i\left(\theta_i\right), \quad \theta_i = \theta_i^* + \theta_{o,i}\,, \tag{3} $$

where θ_i^* is the joint angle and $\theta_{o,i}$ is the joint offset due to misalignment of the home position from the zero joint angles.

2.2. World and Tool Frame Modeling

The MDH approach defines the transformation from the robot base frame to the end-effector or flange frame (${}^{0}\mathbf{H}_n$). However, for path planning, a Cartesian path is typically defined in the world frame and requires an extra world-to-base transformation. Similarly, as the path is defined for the tool/sensor frame rather than the end-effector or flange frame, an extra transformation is required to define the tool/sensor frame. By introducing two additional transformations,

the kinematic model defines the tool/sensor frame with respect to the world frame as

$$ {}^{\mathrm{w}}\mathbf{H}_{n+1}(\boldsymbol{\theta}) = {}^{\mathrm{w}}\mathbf{H}_0 \, {}^{0}\mathbf{H}_n(\boldsymbol{\theta}) \, {}^{n}\mathbf{H}_{n+1} \,, \tag{4} $$

where w represents the world frame and $(n+1)$ represents the tool/sensor frame. These two frames introduce 12 new parameters into the kinematic equations. However, the total number of parameters N required for a complete forward kinematic model is defined in [28] as

$$ N = 4N_R + 2N_P + 6 \,, \tag{5} $$

where N_R is the number of revolute joints and N_P is the number of prismatic joints in the serial kinematic chain. Therefore, the 12 parameters introduced for the definition of the world and tool frames are not independent of the robot parameters. For a 6-DOF robot consisting only of revolute joints, $N = 30$ parameters are required.

Although many researchers have performed calibrations by including dependent parameters in the model, few have defined the transformations by including only the independent parameters using the DH notation [29, 30]. Zhaung et al. introduced the Modified Complete and Parametrically Continuous (MCPC) technique, which is an alternative to DH notation for robot modeling including world and tool/sensor frames with minimal parameter set [31]. As the DH notation is more widespread and the inclusion of the world and tool/sensor frames is essential in practical applications, adopting the notation introduced in [30], we provide a systematic method to extend the MDH table to include the world and tool frames while ensuring a minimal parameter set. These parameters are referred to as the Extended Modified Denavit-Hartenberg (EMDH) parameters herein.

In Fig. 2, the world frame (w) is arbitrarily defined with six parameters or degrees of freedom with respect to the base frame (0). However, two of these parameters will be dependent when considering the calibration model. To select a set of independent parameters, the base frame may be positioned anywhere along the axis of rotation, and any angular offset may be introduced to the joint angle. Therefore, a new base frame $(0')$ may be defined that requires only four parameters. These four parameters must take any arbitrary world frame and align it with the new base frame such that the z-axis is colinear with the joint axis. These four parameters may be selected as $\{\theta_0, d_0, a_0, \alpha_0, \beta_0\}$ with either $d_0 = 0$ or $\beta_0 = 0$ if the world-frame z-axis is parallel or perpendicular to the $0'$ z-axis, respectively. This assignment is equivalent to extending the model parameters by adding an initial 'revolute joint 0' to the convention such that

$$ {}^{\mathrm{w}}\mathbf{H}_{0'} = \mathrm{Rot}_{z,\theta_0}\mathrm{Trans}_{z,d_0}\mathrm{Trans}_{x,a_0}\mathrm{Rot}_{x,\alpha_0}\mathrm{Rot}_{y,\beta_0} \tag{6} $$

defines the transformation between the world frame and the new base frame. Similarly, the tool/sensor frame $(n+1)$ may be arbitrarily defined with six parameters with respect to the end-effector frame (n). However, four of these parameters will be dependent when considering the calibration model because

there is no relative motion between the end-effector frame and the tool frame. It is possible to define an intermediate end-effector frame (n') with parameter set $\{\theta'_{o,n}, d'_n, a'_n, \alpha'_n, \beta'_n\}$ that requires only two additional constraints, $\{\theta_{n+1}, d_{n+1}\}$, to define the tool/sensor frame ($n+1$). Fig. 2 illustrates how the tool/sensor frame can be defined by two independent parameters from the intermediate frame n'. The transformation across the n^{th} joint to the tool/sensor frame is formulated as

$$\begin{aligned} {}^{n-1}\mathbf{H}_{n'} &= \mathrm{Rot}_{z,(\theta'_{o,n}+\theta^*_n)}\mathrm{Trans}_{z,d'_n}\mathrm{Trans}_{x,a'_n}\mathrm{Rot}_{x,\alpha'_n}\mathrm{Rot}_{y,\beta'_n} \\ {}^{n'}\mathbf{H}_{n+1} &= \mathrm{Rot}_{z,\theta_{n+1}}\mathrm{Trans}_{z,d_{n+1}}\,, \end{aligned} \tag{7}$$

with either $d'_n = 0$ or $\beta'_n = 0$ to avoid singularities when the tool/sensor frame is either near-parallel or near-perpendicular to the intermediate end-effector frame. Similar to the world frame assignment, this definition is equivalent to extending and modifying the model parameters, where the tool/sensor frame adds a partial set of parameters. Table 1 lists the EMDH parameters for a general n-DOF serial manipulator, including the world and tool/sensor frames. The independent parameter vector is generated by stacking parameters of the EMDH table such that

$$\boldsymbol{\rho} = \begin{bmatrix} \boldsymbol{\theta}_o{}^{\mathsf{T}} & \mathbf{d}^{\mathsf{T}} & \mathbf{a}^{\mathsf{T}} & \boldsymbol{\alpha}^{\mathsf{T}} & \boldsymbol{\beta}^{\mathsf{T}} \end{bmatrix}^{\mathsf{T}}, \tag{8}$$

where, for an n-DOF robot with revolute joints, $\boldsymbol{\theta}_o \in \mathbb{R}^{n+2}$, $\mathbf{d} \in \mathbb{R}^{n+2-b}$, $\mathbf{a} \in \mathbb{R}^{n+1}$, $\boldsymbol{\alpha} \in \mathbb{R}^{n+1}$, $\boldsymbol{\beta} \in \mathbb{R}^b$ and b is the number of consecutive frames with near-parallel z-axes.

2.3. Measurements

In this section, the method for data collection with robot-mounted measurement devices and the definition of the target workspace for local calibration are respectively discussed.

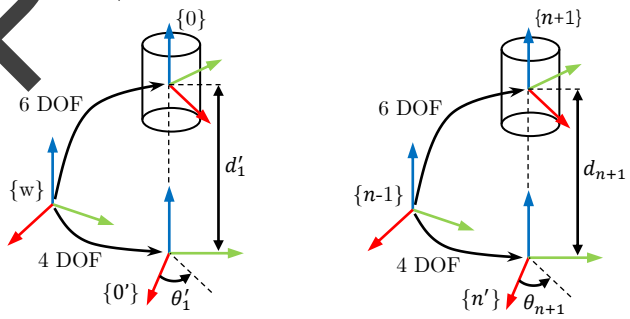

Figure 2: Intermediate frame assignment to remove the dependent parameters. (Left) Frame $0'$ is defined on the z-axis of base frame. (Right) Frame n' is defined on the z-axis of the tool/sensor frame.

Measurements from Robot-Mounted Device

Most calibration methods use an external measurement device to detect the full or partial pose of the end-effector for absolute calibration. However, in the current work, robot-mounted measurement devices are used for constraint-based calibration. These devices collect full or partial spatial information while interacting with a calibration artifact, and the type of artifact defines the constraint for calibration. Considering the measurement output as a point in the sensor/tool frame ${}^{n+1}\mathbf{p}_m$, the estimated world-frame position is

$$\begin{bmatrix} {}^{\mathrm{w}}\hat{\mathbf{p}}_m \\ 1 \end{bmatrix} = {}^{\mathrm{w}}\hat{\mathbf{H}}_{n+1} \begin{bmatrix} {}^{n+1}\mathbf{p}_m \\ 1 \end{bmatrix}, \tag{9}$$

where the estimated transformation from the world to the tool/sensor frame ${}^{\mathrm{w}}\hat{\mathbf{H}}_{n+1}$ is dependent on the parameter vector $\boldsymbol{\rho}$. In this process, the measurement data for calibration consists of the robot joint angles and the sensor output. The sensor output could be a single or a collection of points expressed in the world frame according to (9). The data collection process for two types of sensors used in this study are discussed.

Many industrial robots are equipped with non-contact measurement devices such as cameras and laser scanners to collect spatial data about the object in the robot workspace. In the current work, a laser profile scanner is used, which applies the principle of triangulation for two-dimensional profile detection. A single laser profile consists of a set of points expressed in the laser frame,

$${}^{\ell}\mathbf{p}_m = \begin{bmatrix} x_m & 0 & z_m \end{bmatrix}^{\mathsf{T}}. \tag{10}$$

As the robot moves through its workspace, the robot-mounted laser scanner collects a series of profiles showing the objects in its field of view. Using (9),

Table 1: EMDH Parameters of n-DOF Manipulator

Transformation	θ	d	a	α	β
${}^{\mathrm{w}}\mathbf{H}_{0'}$	$\theta_{o,0}$	d_0	a_0	α_0	β_0
${}^{0'}\mathbf{H}_1$	$\theta'_{o,1} + \theta_1$	d'_1	a_1	α_1	β_1
:	:	:	:	:	:
${}^{i-1}\mathbf{H}_i$	$\theta_{o,i} + \theta_i$	d_i	a_i	α_i	β_i
:	:	:	:	:	:
${}^{n-1}\mathbf{H}_{n'}$	$\theta'_{o,n} + \theta_n$	d'_n	a'_n	α'_n	β'_n
${}^{n'}\mathbf{H}_{n+1}$	θ_{n+1}	d_{n+1}	$\times$	$\times$	$\times$

all collected profiles can be transformed to the world frame to generate a three-dimensional point cloud representation of any object in the workspace.

The second measurement device discussed herein is the force/torque sensor. Many applications require measurement of the interaction force between an object and a robot-mounted tool. Therefore, the robot is equipped with a force/torque sensor, which can be used to implement a touch-off process to create physical contact with a calibration artifact. The robot is programmed to move the tool close to the artifact and then slowly approach the artifact. When the contact force crosses a designated threshold, the robot stops and the robot pose is recorded. Each touch-off is considered a partial measurement of the tool tip location expressed in the tool frame as

$$^{\mathrm{t}}\mathbf{p}_m = \begin{bmatrix} 0 & 0 & t_m \end{bmatrix}^{\mathsf{T}}, \tag{11}$$

where t_m is the tool length.

Local Data Collection

Let the robot workspace $\mathcal{T} \subset SE(3)$ be the set of all feasible end-effector poses $\mathbf{H}_{ee}$ of the form

$$\mathbf{H}_{ee} = \begin{bmatrix} \mathbf{R}_{ee} & \mathbf{p}_{ee} \\ \mathbf{0} & 1 \end{bmatrix}, \tag{12}$$

where $\mathbf{p}_{ee}$ and $\mathbf{R}_{ee}$ represent the Cartesian position and orientation of the end-effector, respectively. Global calibration is typically performed by collecting random poses throughout the workspace.

In contrast, local calibration aims at a specific target subarea of the workspace $\mathcal{L} \subset \mathcal{T}$. To achieve best results, local calibration should be performed with measurement poses that are as close to the robot poses used in the actual application as possible. As industrial robots are typically made of a series of links articulated by rotary joints, positional errors demonstrate more similarity when the robot pose is closer in the joint space rather than the task space [24]. Therefore, the definition of the subset for local calibration should not only restrict the Cartesian position of the tool/sensor frame origin, but should also consider the end-effector orientation. The target workspace $\mathcal{L}$ is defined as

$$\mathcal{L} = \left\{ \begin{bmatrix} \mathbf{R}_{ee} & \mathbf{p}_{ee} \\ \mathbf{0} & 1 \end{bmatrix} \in \mathcal{T} \;\middle|\; \mathbf{R}_{ee} \in \mathcal{R}_d \,,\; \mathbf{p}_{ee} \in \mathcal{P}_d \right\}, \tag{13}$$

where $\mathcal{R}_d$ is the desired set of end-effector orientations and $\mathcal{P}_d$ is the desired set of end-effector positions in Cartesian space. For a machining application, the desired position subset can be defined based on the location of the clamping system and the maximum size of the workpiece. The position subset $\mathcal{P}_d$ may be defined as a cube in Cartesian space as

$$\mathcal{P}_d = \Big\{ \mathbf{p}_{ee} := [p_x \;\; p_y \;\; p_z] \in \mathbb{R}^3 \;\Big|\; p_x \in \mathcal{B}_x \,,\;\; p_y \in \mathcal{B}_y \,,\;\; p_z \in \mathcal{B}_z \Big\}, \tag{14}$$

where $\mathcal{B}_x$, $\mathcal{B}_y$, and $\mathcal{B}_z$ are the allowable real intervals on the x-, y- and z-coordinates, respectively.

Although industrial robots have high flexibility in achieving desired tool orientations, certain applications may impose restrictions on tool orientation. For instance, constant tool orientaion maybe desirable for manufacturing of sheetmetal parts. Other applications may allow bounded deviation of the tool axis from a predifined dominant orientation to allow machining more complex features or creating holes and chamfers. A practical method for defining the orientation subset $\mathcal{R}_d$ is to restrict the tool axis within a cone-shaped space as

$$\mathcal{R}_d = \Big\{ \mathbf{R}_{ee} := [\mathbf{x}_{ee} \;\; \mathbf{y}_{ee} \;\; \mathbf{z}_{ee}] \in SO(3) \;\Big|\; \cos^{-1}({\mathbf{z}_{ee}}^{\mathsf{T}} \mathbf{z}_c) \leq \psi_c/2 \Big\}, \tag{15}$$

where $\mathbf{z}_c$ is the cone axis and ψ_c the the opening angle of the cone.

2.4. Parameter Identification

The model generated in Section 2.2 provides the pose of the tool/sensor frame relative to a world frame. The goal of the parameter identification step is to find numerical values for the EMDH parameters to optimize the accuracy of the generated model. In this section, the measurement error and cost functions are defined for both open-loop calibration with full pose measurements and closed-loop calibration with partial measurements collected using robot-mounted measurement devices as discussed in Section 2.3.

Open-Loop Calibration

Most calibration methods use an external measurement device to measure the full or partial pose of the end-effector frame. For measurement m, the full pose of the end-effector frame with respect to the world frame can be expressed using a transformation matrix as

$${}^{\mathrm{w}}\mathbf{H}_m = \left[\begin{array}{ccc:c} \mathbf{x}_m & \mathbf{y}_m & \mathbf{z}_m & \mathbf{p}_m \\ \hdashline 0 & 0 & 0 & 1 \end{array}\right], \tag{16}$$

where $\mathbf{x}_m$, $\mathbf{y}_m$ and $\mathbf{z}_m$ are the orthonormal vectors which represent the orientation of the end-effector, and $\mathbf{p}_m$ is the position vector. The position error is simply defined as

$$\mathbf{e}_p = \mathbf{p}_m - \hat{\mathbf{p}}_m\,, \tag{17}$$

where $\hat{\mathbf{p}}_m$ is the estimated end-effector position.

Assuming small errors between the measurement and model output, orientation error can be directly calculated from the transformations as [32]

$$\mathbf{e}_o = \frac{1}{2}(\mathbf{x}_m \times \hat{\mathbf{x}}_m + \mathbf{y}_m \times \hat{\mathbf{y}}_m + \mathbf{z}_m \times \hat{\mathbf{z}}_m) \tag{18}$$

where $\hat{\mathbf{x}}_m$, $\hat{\mathbf{y}}_m$ and $\hat{\mathbf{z}}_m$ are the orthonormal vectors representing the estimated orientation. The total error for each measured pose is considered as the sum of the squared Euclidean norms of position and orientation errors such that

$$\mathbf{e}_m = \|\mathbf{e}_p\|^2 + \|\mathbf{e}_o\|^2, \tag{19}$$

where $\|\bullet\|$ is the Euclidean norm operator. If SI units are used, no scaling is required as the positional error in meters and orientation error in radians are directly comparable for human-sized arms [4].

Closed-Loop Calibration

The method proposed herein uses robot-mounted measurement devices to collect data about an artifact, which falls under the constraint-based or closed-loop calibration. A physical or virtual restriction in the robot workspace is used to constrain one or more points attached to the tool/sensor frame. The constraint could be either a point in space presented by the sharp tip of a cone-shaped object, a line presented by intersection of two artifact surfaces or a virtual laser projection, a plane, a cylinder, or a sphere. The method proposed here uses calibration artifact surfaces as planar constraints. Any plane k in space can be mathematically represented by a unit normal vector $\mathbf{n}_k$ and an offset value d_k. The constraint equation for any point ${}^{\mathrm{w}}\mathbf{p}_m \in k$ is defined as

$$\mathbf{n}_k^{\mathsf{T}}\, {}^{\mathrm{w}}\mathbf{p}_m - d_k = 0, \tag{20}$$

where ${}^{\mathrm{w}}\mathbf{p}_m$ is the coordinate vector of the point expressed in the world frame. In the presence of parameter inaccuracies, the estimated position of the measurement point ${}^{\mathrm{w}}\mathbf{p}_m$ may violate the constraint equation. The estimated position is a function of the parameter vector $\boldsymbol{\rho}$ and is calculated according to (9). The normal distance of the measurement ${}^{\mathrm{w}}\hat{\mathbf{p}}_m$ from the plane k is considered as the measurement error and is calculated as

$$e_m = \mathbf{n}_k^{\mathsf{T}}\, {}^{\mathrm{w}}\hat{\mathbf{p}}_m - d_k\,. \tag{21}$$

By differentiating the error function with respect to the robot parameters and vertically stacking all the measurements, the identification Jacobian is defined as

$$\mathbf{J} = \begin{bmatrix} \frac{\partial e_1}{\partial \boldsymbol{\rho}} & \frac{\partial e_2}{\partial \boldsymbol{\rho}} & \cdots & \frac{\partial e_m}{\partial \boldsymbol{\rho}} & \cdots & \frac{\partial e_M}{\partial \boldsymbol{\rho}} \end{bmatrix}^{\mathsf{T}}, \tag{22}$$

where M is the number of measurements. The Jacobian is used to calculate observability of parameters [4]. In the identification step, the optimal parameters $\boldsymbol{\rho}^*$ are identified by

$$\boldsymbol{\rho}^* = \underset{\boldsymbol{\rho}\in\mathbb{R}^N}{\operatorname{argmin}} \|\mathbf{e}\|, \quad \mathbf{e} = \begin{bmatrix} e_1 & e_2 & \dots & e_M \end{bmatrix}. \tag{23}$$

To evaluate the effectiveness of the proposed methods, their implementation in a robotic machining application is presented in Section 3.

3. Application of Methods

The proposed methods are implemented in the calibration of a robotic machining system, which includes:

- DENSO VS-6556W 6-DOF manipulator;
- 350W NSK spindle with 1/8-inch 2-flute carbide end mill;
- Micro-Epsilon scanCONTROL 2950-50 profile scanner;
- ATI Gamma six-axis force/torque sensor; and
- Vise with locating edges.

Fig. 3 shows a close-up of the spindle, end mill, and various views of the experimental setup. A variable-helix end mill was selected to reduce chatter.

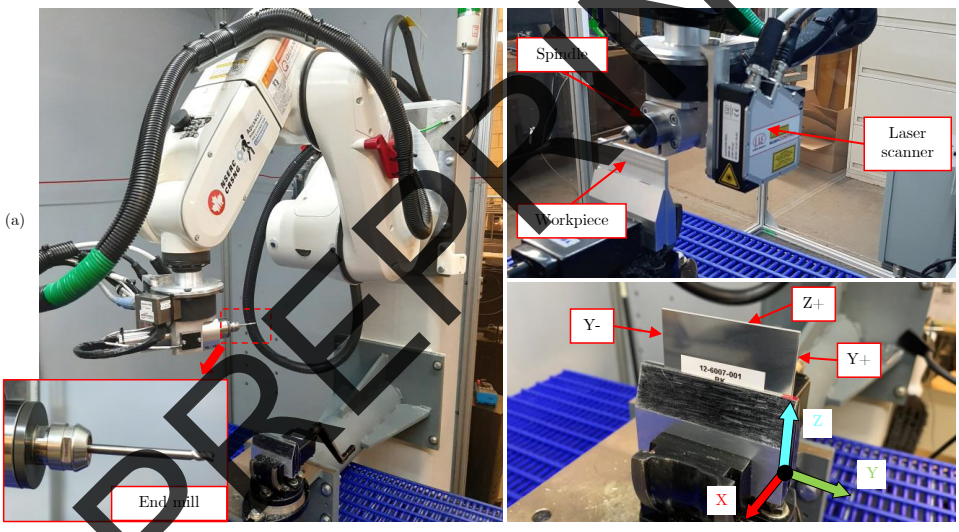

Figure 3: Experimental setup, including (a) the robotic system and end mill, (b) key components, and (c) workpiece with labeled edges.

The experimental machining application is designed to cut the edges of a sheet metal workpiece to a desired depth of cut. Throughout the process, a three-dimensional model of the workpiece in the standard STL file format is used whenever there is a need for geometrical information. This three-dimensional model is referred to as the STL model. Fig. 4 summarizes the process for the experimental machining application. The steps of the process are described as:

- *Load*: The workpiece is loaded into a vise.
- *Scan*: The workpiece is scanned with the robot-mounted laser scanner to construct a unified point cloud as explained in Section 2.3.

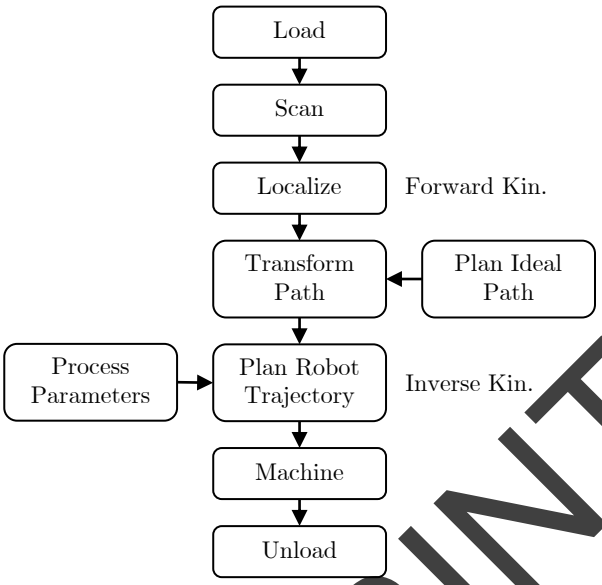

Figure 4: The kinematic control machining process.

- *Localize*: The workpiece pose is estimated with a localization process, which is described in Section 3.2.
- *Plan Ideal Path*: The ideal tool path is defined from the STL model in the local frame such that an end mill follows the periphery with a specified depth of cut.
- *Transform Path*: The ideal path is transformed from the local frame of the STL model to the world frame using the pose estimation from the localization step.
- *Plan Robot Trajectory*: A Cartesian trajectory is defined based on the tool path and process parameters (i.e., feedrate, etc.). The joint-space trajectory is generated by applying the inverse kinematic model.
- *Machine*: The robot follows the joint space trajectory with kinematic control to perform the machining operation.
- *Unload*: Finally, the processed workpiece is removed.

A locally-calibrated model of the robot/laser kinematic chain is used to convert the laser scanner output to the world-frame point cloud in the *Scan* step. This model is referred to as the Local Robot/Laser Model (LRL Model), and the calibration process is discussed in Section 3.1. Similarly, another locally-calibrated model is used for the robot/tool kinematic chain to convert the local/ideal path to the world frame in the trajectory planning step. This model

is referred to as the Local Robot/Tool Model (LRT Model), and the calibration process is discussed in Section 3.3. To compare the effectiveness of local calibration, a Global Robot/Tool Model (GRT Model) is calibrated for the robot/tool chain. The GRT model is discussed in Section 3.4.

3.1. Local Robot/Laser (LRL) Model

The robot is equipped with a laser profile scanner to act as a non-contact measuring device. The robot/laser model is calibrated by scanning an artifact and identifying parameters as described in Sections 2.3 and 2.4. Fig. 5 shows a simplified schematic of the robot with key link dimensions, joint variables θ_i, positive directions of rotation, tool frame t, and laser frame l.

For local calibration, the scan path must be defined such that

$$\mathbf{n}_k^{\mathsf{T}}\,\mathbf{z}_m < 0\,, \tag{24}$$

where $\mathbf{z}_m$ is the sensor z-axis defined in (16) and $\mathbf{n}_k$ is the normal vector of the surface being scanned. This constraint is necessary to ensure the surface is visible in laser field of view. If the orientation of the end-effector is constant, not all required surfaces are visible. To address this issue, a two-segment path is designed to scan the object with two different sensor orientations. Consequently, the faces that are not visible in the first segment are scanned in the second segment. The two segments of the scan path can be described as two local subsets of the workspace according to (13) with position boundaries listed in Table 2 and desired constant orientations defined as

$$\begin{aligned}
\mathcal{R}_{\ell 1} &= \{\mathbf{R}_{\ell 1}\}\,,\ \mathbf{R}_{\ell 1} = \mathrm{Rot}_{z,\pi/2}\,\mathrm{Rot}_{x,-\pi/10}\,\mathrm{Rot}_{z,-9\pi/10} \\
\mathcal{R}_{\ell 2} &= \{\mathbf{R}_{\ell 2}\}\,,\ \mathbf{R}_{\ell 2} = \mathrm{Rot}_{z,-\pi/2}\,\mathrm{Rot}_{x,-\pi/10}\,\mathrm{Rot}_{z,9\pi/10}\,,
\end{aligned} \tag{25}$$

where subscripts $\ell 1$ and $\ell 2$ refer to the first and second segment respectively. The trajectory was planned for cartesian velocity of 4 $\mathrm{mm\,s^{-1}}$ which for the scan frequency setting of 100 Hz results in the resolution of 40 µm between laser profiles.

The calibration is performed by scanning the calibration artifact, a combination of two 1-2-3 blocks, in a series of poses within the vise. A 1-2-3 block is a common tool made of hardened steel with dimensions $1 \times 2 \times 3$ inch within

Table 2: Position Boundaries for Calibration Measurements

	$\mathcal{P}_d$		
Model	$\mathcal{B}_x$ [mm]	$\mathcal{B}_y$ [mm]	$\mathcal{B}_z$ [mm]
LRL 1	660	$[-20, 120]$	1342
LRL 2	662	$[-2, 137]$	1343
LRT	$[580, 610]$	$[-80, 50]$	$[1150, 1275]$
GRT	$[480, 840]$	$[-130, 130]$	$[1060, 1560]$

0.0002 inch accuracy. Constraints are defined to relate points detected on each block face to the known/assumed location of each face. Fig. 6 shows several

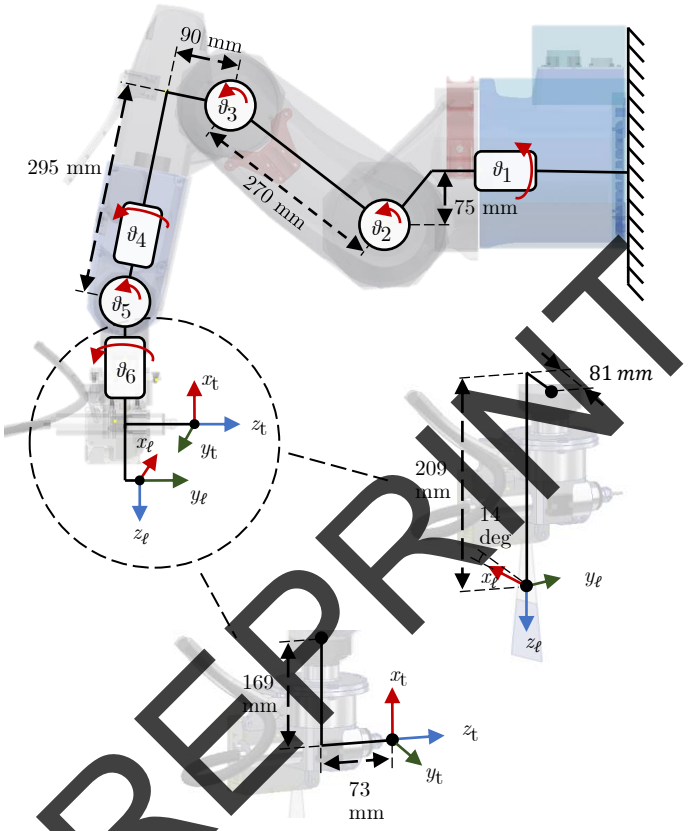

Figure 5: Simplified schematic of the robot with key link dimensions, joint variables θ_i, positive directions of rotation, tool frame t, and laser frame l.

configurations created by placing two 1-2-3 blocks together. A frame is assigned to the vise with origin at the locating edge. As one of the blocks in each configuration is placed against the locating edge, the normal vector and plane offset

Table 3: Surface constraints used in calibration

k	1	2	3	4	5	6	7	8	9
n_k	**k**	**k**	**j**	**k**	**i**	**i**	**j**	**j**	**j**
d_k [inch]	2	4	-3	3	-1	0	-4	-2	0

of each constraint face is known based on of the block dimensions. Table 3 lists the normal vector $\mathbf{n}_k$ and the plane offset d_k for all the faces used in the calibration process illustrated in Fig. 6, where $\mathbf{i}$, $\mathbf{j}$ and $\mathbf{k}$ are the standard basis of the vise frame.

Each laser profile consists of 1280 points along the laser line projected on the calibration artifact. Not all the profiles and points are valid measurements as the projected laser line may not be on the object or partially covering it during the scan. The points are filtered using bounding boxes defined around the calibration artifact to select the appropriate measurement data set for calibration. Moreover, relative orientation of scan projection, artifact surface properties and corner conditions can generate noise/outliers in the measurements. Appropriate outlier rejection methods were used to filter out points that are a certain threshold away from the assumed artifact surface.

For the experimental setup considered herein, the robot has near-parallel revolute joints on links 2 and 3. Moreover, the laser frame z-axis is near parallel to the axis of rotation on link 6 of the robot. Therefore, the parameter vector of the robot model is of the form presented in (8) where $\mathbf{d} = \begin{bmatrix} d_0 & d_1 & d_3 & d_4 & d_5 & d_7 \end{bmatrix}^\mathsf{T}$ and $\boldsymbol{\beta} = \begin{bmatrix} \beta_2 & \beta_6 \end{bmatrix}^\mathsf{T}$. The Jacobian matrix calculated with (22) has a rank of 30, which indicates that all parameters are identifiable.

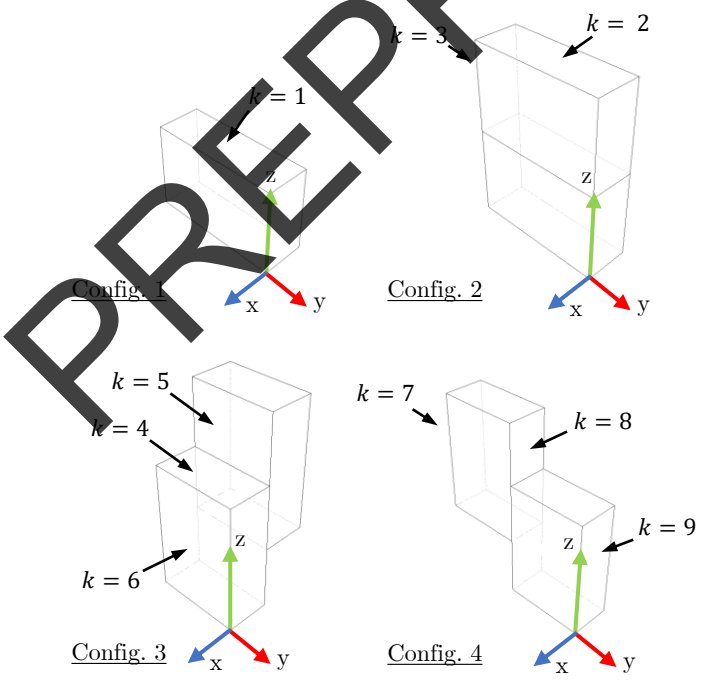

Figure 6: 1-2-3 block configurations used to define absolute coordinate constraints. The coordinate frame shown in each configuration shows where the blocks are fixed in the locating edge of the vise and is aligned with the world coordinate frame.

As discussed in Section 2.3, selection of the target area for local calibration affects the level of achievable accuracy. Although the laser scanning path was designed to approach a small target area in the task space, the two scan segments could be considered two separate subsets as the orientation of the end-effector is significantly different for each segment. Including the measurements from both segments, a model named LRL–1/2 was calibrated; however, as expected, the accuracy is not satisfactory. Therefore, two separate local models LRL–1 and LRL–2 were calibrated for each segment. Hereafter, LRL model is the combination of both local models as each is used to transform the data collected in the corresponding segment to the world frame to generate the scan output.

Using the locally-calibrated models, it is possible to scan a workpiece, transform the scan data into the world frame, and accurately determine the workpiece pose via a localization process. This process is briefly discussed in the following subsection.

3.2. Localization

Given a scan of the workpiece in the world frame, a localization process is performed to find the optimal pose of the workpiece as

$$ {}^{\mathrm{w}}\hat{\mathbf{H}}_{\mathrm{v}} = \underset{\mathbf{H}\in SE(3)}{\operatorname{argmin}} \sum_{i=1}^{M} \left\| \mathbf{H}^{-1} \begin{bmatrix} {}^{\mathrm{w}}\mathbf{p}_{\mathrm{c},i} \\ 1 \end{bmatrix} - \begin{bmatrix} {}^{\mathrm{v}}\mathbf{p}_{\mathrm{s},i} \\ 1 \end{bmatrix} \right\|^2 \tag{26} $$

where ${}^{\mathrm{w}}\hat{\mathbf{H}}_{\mathrm{v}}$ represents the estimated pose of the workpiece relative to the world frame, ${}^{\mathrm{w}}\mathbf{p}_{\mathrm{c},i}$ is the i^{th} point in the world-frame scanned point cloud, and ${}^{\mathrm{v}}\mathbf{p}_{\mathrm{s},i}$ is the matching local-frame point on the STL model that is closest to ${}^{\mathrm{w}}\mathbf{p}_{\mathrm{c},i}$ after applying the transformation $\mathbf{H}^{-1}$ to convert to the local frame. The optimization is performed with built-in MATLAB functions.

Fig. 7 illustrates the point-to-plane method used to match points in the cloud to points on the STL model in the local frame. For each point $\mathbf{p}_{\mathrm{c},i}$, a normal vector $\mathbf{n}_{\mathrm{c},i}$ is computed by fitting a plane to the k-nearest-neighbors. These normal vectors are compared to the normal vectors of the STL model $\mathbf{n}_{\mathrm{s},j}$ to match each point with a corresponding face/plane, and the point is projected onto the face to define the matching point $\mathbf{p}_{\mathrm{s},i}$.

Fig. 8 shows an example of the localization process. The STL model is represented as a square with black edges and the point cloud is shown as red points. The local frame of the STL model is shown in the center of each image with labelled x-y-z axes. In the left image, the initial estimate of the pose yields high point-to-plane errors, which are indicated by the length of the red lines that join points in the cloud to the matching points on the STL model. In the right image, the final estimate demonstrates the result of the localization process as the STL model is closely matched with the point cloud and errors are minimized.

After the workpiece location is determined, a robot/tool model is required to perform the machining operation. In the following subsection, the local calibration of the robot/tool model is discussed.

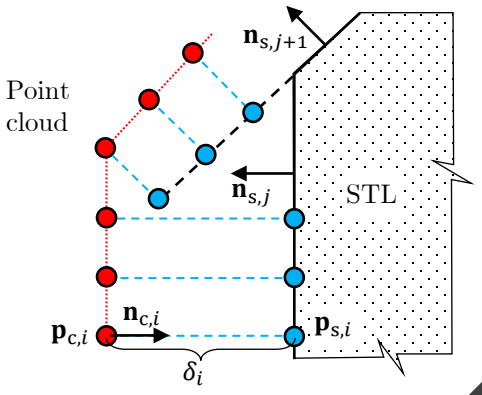

Figure 7: The point-to-plane matching process. For each point in the cloud a matching point is identified to calculate the point-to-plane error.

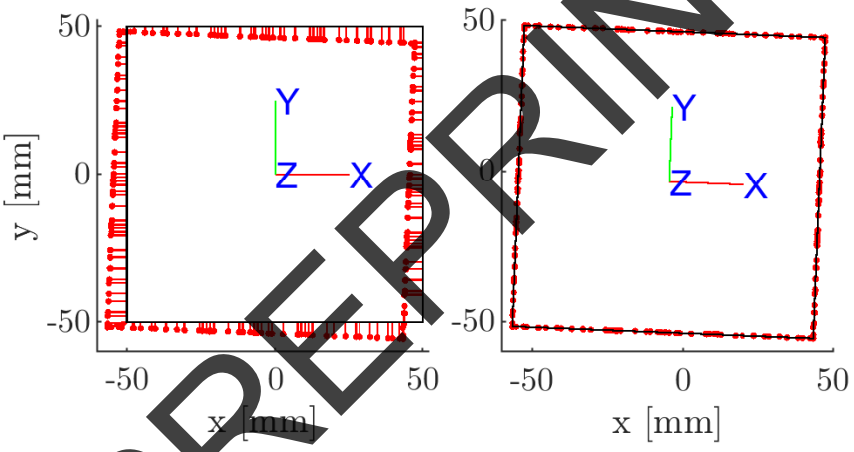

Figure 8: An example of the localization process for a square box. Left: Initial estimate of the box pose yields high point-to-plane error shown using red lines. Right: Final pose estimate after localization minimizes the deviation of point cloud from STL surfaces.

3.3. Local Robot/Tool (LRT) Model

To improve machining accuracy, the robot/tool model used for path planning must also be calibrated. The robot/tool kinematic chain was calibrated using the touch-off process discussed in Section 2.3. For this specific application, the local region for collecting measurement data was selected to cover the robot poses in the actual trajectory used during the machining process. In the case study addressed here, the parts are made out of sheet metal and are held in a vise. Tool orientation is commanded to be along the normal vector of the sheet metal plane. Therefore, the target workspace is defined using (13) for position

limits provided in Table 2 and an orientation defined as

$$\mathcal{R}_{\mathrm{t}} = \{\mathbf{R}_{\mathrm{t}}\}\,, \;\; \mathbf{R}_{\mathrm{t}} = \mathrm{Rot}_{y,-\pi/2}\,. \tag{27}$$

In the robot/tool chain, only links 2 and 3 have near-parallel revolute joints and the parameter vector is of the form presented in (8) with $\mathbf{d} = \begin{bmatrix} d_0 & d_1 & d_3 & d_4 & d_5 & d_6 & d_7 \end{bmatrix}^{\mathsf{T}}$ and $\boldsymbol{\beta} = [\beta_2]$. Moreover, the artifact is scanned with the calibrated LRL Model to determine the absolute measurements and ensure correspondence between LRL and LRT models that are used in position sensing and trajectory planning, respectively.

For measurements of the y- and z-faces of the block, the cylindrical surface of the tool shank is in contact, whereas the tool tip is in contact with the block while measuring the x-face. Therefore, the planar error equation (21) for the y- and z-faces was modified to include the tool radius as

$$e_m = \mathbf{n}_k^{\mathsf{T}}\, \hat{\mathbf{p}}_m - d_k - r\,, \tag{28}$$

where r is the tool radius.

In the current setup, data was collected for four locations of a 1-2-3 block held by the vise. A total of 260 measurements were collected and used in parameter identification. Touch points were planned with a resolution of 2.5 mm.

The rank of the Jacobian matrix, calculated according to (22), shows that the maximum number of observable parameters is 29. The unobservable parameter is θ_7, which corresponds to rotation about the tool axis. This result is expected as the cylindrical tool does not provide any constraint about the tool axis.

3.4. Global Robot/Tool (GRT) Model

To benchmark the performance of the local calibration, a global calibration was first performed with an NDI Optotrak Certus system with measurement accuracy of up to 0.1 mm [33], which tracked the pose of active markers attached to the end-effector. The robot was guided through a series of poses while the joint angles and the corresponding Optotrak data were collected. Two sets of poses were used to collect the data. The measurement set was collected by moving the robot inside a 300 mm target cube, which covers the local subset for LRT model defined in (27) while randomly changing the tool orientation. Lastly, a digitizing probe [33] was used to define the world and tool frame. The world frame was defined at the locating edges of the vise, and it was identified by probing the three orthogonal surfaces of the jaws. The tool frame was defined at the tool base on the spindle and is identified by probing the spindle surface and tool tip. The measurement error vector was calculated using (19) and was used in (23) to identify the GRT model parameters.

4. Results and Discussion

In Section 4.1, the calibration results for the globally-calibrated and locally-calibrated models are presented, and the improvements in accuracy are discussed. In Section 4.2, the results of the machining application with the locally-calibrated models are presented.

4.1. Calibration Results

The nominal parameter set is reported in Table 4 and consists of the nominal robot, world-frame, and tool/sensor-frame parameters. The nominal robot parameters are provided by the manufacturer and are illustrated in Fig. 5, whereas the world and tool/sensor frame parameters are assigned from manufacturing drawings of the experimental setup. During calibration, four parameter sets are identified using the methods described in Section 2, and the achieved accuracy for each parameter set is discussed in this section.

Using the absolute measurements collected with the Optotrak system, a global model (GRT) is calibrated with the method described in Section 3.4. The identified parameters are reported in Table 4. Fig. 9 shows the position and orientation error histogram before and after calibration. The calibrated GRT model reduces the average positional error from 8.02 mm to 0.80 mm and orientation error from 1.86 deg to 0.36 deg. Although this improvement is significant, it is not adequate for the machining application considered herein.

To improve the sensing accuracy of the system, a local model (LRL) is calibrated using 1-2-3 blocks as described in Section 3.1. The depth errors of the point cloud with respect to the constraint surfaces of the 1-2-3 blocks are summarized in Table 5. Including both segments of the scan path in a single calibration (LRL 1/2) results in a mean error of 0.22 mm, which does not achieve the desired accuracy for the application. Therefore, separate models are calibrated for each segment of the scan path (LRL 1, LRL 2). Both calibrated models show excellent accuracy as the mean and standard deviation of error are well below the expected accuracy for the application. The calibrated parameters for each path segment are reported in Table 4.

Finally, to improve positional accuracy of the tool tip, another local model (LRT) is calibrated as described in Section 3.3. The identified parameters are

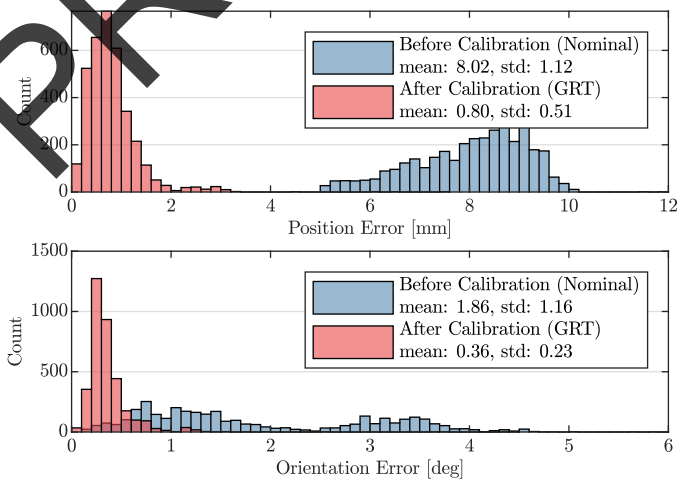

Figure 9: Positional error before and after the calibration for the global model.

reported in Table 4, and Table 5 summarizes the average and standard deviation of errors achieved with this model. For comparison, Fig. 10 shows the error histogram for the nominal, globally-calibrated and locally-calibrated models for the measurements collected from touch-off tests on the y and z faces of the 1-2-3 blocks. The LRT Model shows significant improvement compared with the nominal and GRT models. The average and standard deviation of errors are reduced to 0.04 mm and 0.04 mm respectively. The majority of errors are within ± 0.2 mm and the average tool tip position is successfully corrected.

4.2. Machining Accuracy

To confirm machining accuracy, a series of experiments are performed on rectangular aluminum coupons according to the process illustrated in Fig. 4. The coupons are approximately $2.5 \times 3.0 \times 0.064$ inch and are positioned in the vise such that three exposed edges may be scanned and machined.

After positioning the coupon in the vise, it is scanned with the robot-mounted laser scanner. The corresponding point cloud is generated using the LRL model to transform scan profiles to the world frame. Using the localization process discussed in Section 3.2, the workpiece pose is determined from this point cloud. To verify localization accuracy prior to machining the coupon, touch-off tests are performed with the shank of the tool as described in Section 2.3. These tests demonstrate the combined accuracy of the LRL and LRT models, as well as the localization algorithm. Fig. 11 shows the touch-off and localization errors for a typical test coupon. Positive depth indicates a point inside the nominal STL model used for localization. Considering the errors for the y-edges of the coupon, the mean values are nonzero for both the point cloud and the tool touch-offs. This shift indicates the difference in size between the actual coupon and its nominal STL model. The values indicate an average size difference of up to 0.15 mm in coupon width. The localization automatically adjusts the y-offset to make the errors symmetric. For these experiments, only the top edge affects the z-offset during localization; therefore, the height of the

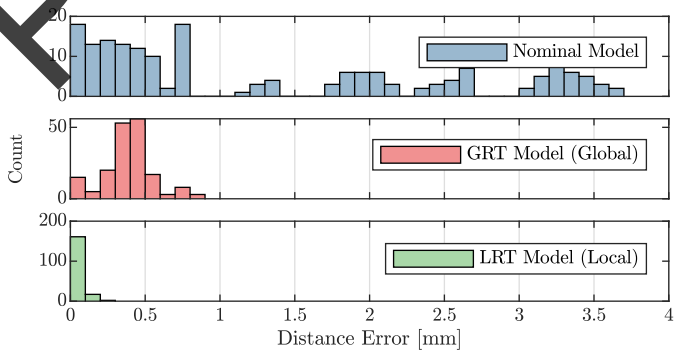

Figure 10: Distance error histogram for Nominal, GRT and LRT models in the 1-2-3 block touch-off tests.

coupon does not affect the localization accuracy. As shown in the plot of errors on the z-edge, the point cloud mean is zero which shows the localized point cloud has shifted to the center of the top surface.

Table 4: Summary of robot parameter sets for robot/tool models (nominal, global and local) and robot/laser models (nominal, local-segment 1 and local-segment 2).

	Robot/Tool Models			Robot/Laser Models		
Parameter	Nom	GRT	LRT	Nom	LRL 1	LRL 2
θ_0 [deg]	90	89.93	90.70	90	90.20	89.89
θ_1 [deg]	-90	-89.48	-89.50	-90	-89.29	-89.39
θ_2 [deg]	90	89.75	90.31	90	89.60	89.70
θ_3 [deg]	-90	-89.66	-90.28	-90	-89.72	-90.11
θ_4 [deg]	0	1.06	0.47	0	1.47	1.85
θ_5 [deg]	0	-0.03	-0.06	0	0.44	-0.21
θ_6 [deg]	-61	-59.88	-59.09	-47	-47.11	-47.19
θ_7 [deg]	90	91.08	91.08	-14	-14.52	-14.56
d_0 [mm]	1564	1561.70	1557.67	1564	1553.42	1535.88
d_1 [mm]	335	323.41	330.36	335	331.06	325.13
d_3 [mm]	0	-0.55	-0.08	0	3.55	4.20
d_4 [mm]	295	294.07	291.18	295	288.69	291.70
d_5 [mm]	0	0.22	-1.41	0	-0.52	-3.31
d_6 [mm]	169	168.78	166.30	×	×	×
d_7 [mm]	73	55.90	45.60	209	199.08	190.24
a_0 [mm]	0	-0.94	-4.08	0	-0.40	0.35
a_1 [mm]	75	77.31	76.61	75	80.75	71.69
a_2 [mm]	-270	-270.31	-269.02	-270	-269.12	-261.80
a_3 [mm]	-90	-91.80	-90.07	-90	-89.92	-94.87
a_4 [mm]	0	0.14	-3.49	0	1.27	-10.89
a_5 [mm]	0	-0.26	3.83	0	-2.55	0.25
a_6 [mm]	-0	0.99	3.68	81	70.48	82.68
α_0 [deg]	90	89.80	89.81	90	89.43	89.67
α_1 [deg]	-90	-90.16	-89.86	-90	-89.65	-88.98
α_2 [deg]	0	-0.11	0.01	0	-0.15	-0.31
α_3 [deg]	90	90.40	90.39	90	90.31	90.39
α_4 [deg]	-90	-92.11	-92.18	-90	-91.27	-92.05
α_5 [deg]	90	91.77	91.86	90	91.92	91.30
α_6 [deg]	-90	-89.85	-90.08	-0	0.17	-0.76
β_2 [deg]	0	-0.10	-0.33	0	-0.38	-0.15
β_6 [deg]	×	×	×	-0	-0.16	0.21

× Parameter is not applicable.

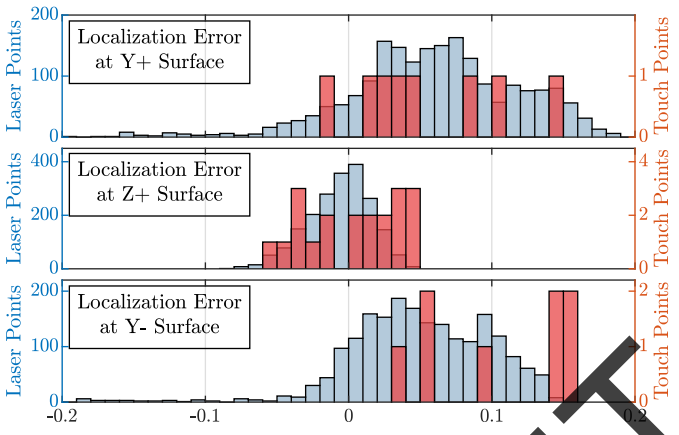

Figure 11: Depth Error histogram for laser scanner and touch-off test outputs on the sample coupon

Finally, the ideal kinematic control path is planned offline with specified depths of cut (−0.15, 0, 0.15 and 0.2 mm) for each of the exposed coupon edges. The path is transformed from the local frame to the world frame and converted to joint angles via the locally-calibrated inverse kinematic model (LRT). The spindle is activated and the joint angle set-points are followed via kinematic control. For all experiments, a feed rate of 10 mm/s and spindle speed of 25000 RPM are applied. Each coupon was machined gradually with four different depths of cut along each edge. For a visual indication of how much material was removed, coupon edges were marked red before each machining test. Fig. 13 shows the coupon edges after the commanded depths of 0 mm and 0.15 mm. The tool was in contact with the z-edge for most of the path, and the edge was completely clean at 0.15 mm depth of cut. For both y-edges, the tool barely touched the coupon at 0 mm depth of cut. This error occurs because the

Table 5: Summary of the errors for calibrated models

	Nominal Error [mm]		Calibrated Error [mm]	
Model	mean	std	mean	std
LRL 1/2	-3.58	4.97	-0.22	0.75
LRL 1	-4.14	6.47	-0.00	0.03
LRL 2	-2.62	2.33	0.00	0.06
GRT	1.34	1.21	0.39	0.17
LRT	1.34	1.21	0.04	0.04

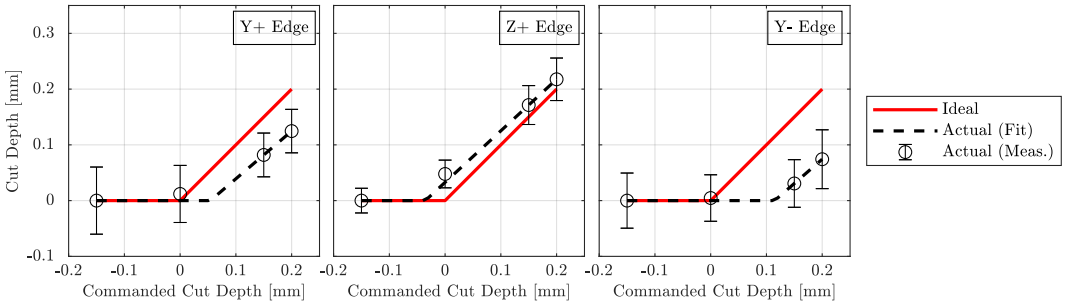

Figure 12: The actual (from point cloud means) vs ideal depth.

tool path is designed from the nominal STL model while the actual workpiece was slightly smaller in width as discussed above.

After each cut, the coupon is scanned with the laser scanner. Fig. 12 compares the commanded and actual depth of cut on a typical coupon. The actual depth is the mean of the point cloud generated from laser scans after each cut. The point cloud distribution is illustrated using the error bars on each data set. The horizontal distance between the line fitted to the actual depth and the line representing the commanded value is an indication of the tool positional accuracy. The same machining experiment was performed on seven coupons. We consider the difference between the measured depth from the laser scans and the commanded depth as the machining error. Table 6 summarizes the maximum and mean machining error for the all experiments. The machining accuracy is considered the maximum measured error for all the coupons and is less than 0.15 mm.

The point cloud distribution on the y-edges shows that the tool does not engage the workpiece at -0.15 mm and 0 mm depth of cut, which confirms that the actual width of the workpiece is slightly smaller than the nominal STL model. The actual depth of cut corresponds to the commanded value for the 0.15 mm and 0.2 mm tests. The maximum error between the commanded and measured depth is on the negative y-edge and is due to the robot/tool model error.

Table 6: Machining errors for the experimental coupons

	mean [mm]	max [mm]
Y+ Edge	0.07	0.15
Z+ Edge	0.08	0.05
Y- Edge	0.07	0.14

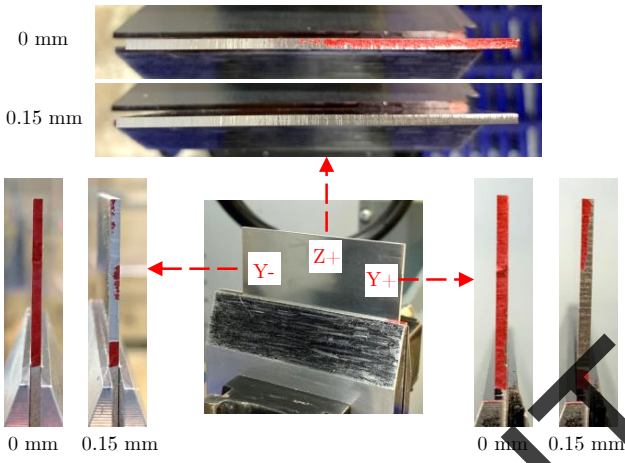

Figure 13: Rectangular coupon edges after depth of cut of 0 and 0.15 mm

5. Conclusion

This paper presented a method for high-accuracy local calibration of industrial robots with robot-mounted measurement devices. The developed methodology uses locally-calibrated models instead of global models. The calibration process does not require external measurement devices, and it can be used to calibrate both the robot/tool and robot/sensor kinematic chains in any target workspace. Common and inexpensive 1-2-3 blocks were used as calibration artifacts in this example; however, the process may be adapted to a variety of artifacts. Local calibration significantly improves model accuracy and, consequently, workpiece localization and machining accuracy in the case study that was considered herein.

The methodology was demonstrated through experiments with a DENSO VS-6556W robot. Locally-calibrated models for the robot/laser chain were used for workpiece localization, and a localization accuracy of ± 0.1 mm was achieved. After localization, a locally-calibrated model for the robot/tool chain was used for path planning. Kinematic control machining experiments were conducted by executing the desired trajectory in position control mode to machine several rectangular coupons. The path was planned to gradually cut the coupon edges, and laser scans were used to quantify the tool tip positional accuracy. The results demonstrated that a positional accuracy of ± 0.15 mm could be achieved for the tool tip using the locally-calibrated models and the process described herein.

The developed methodology can be extended to different areas of the workspace by repeating the process and introducing additional local models. For processes that have higher loads on the end-effector or larger machining forces, joint flexibility may worsen the achievable accuracy. This issue can be addressed by including the joint stiffness in the robot model.

Acknowledgment

We acknowledge the support of the Natural Sciences and Engineering Research Council of Canada (NSERC), [grants RGPIN-2017-06967, RGPIN-2015-04169, and CRDPJ-514258-17]. The authors also acknowledge the financial and technical support from Arnprior Aerospace Inc. (AAI). The authors acknowledge the technical support and feedback of Steffan Lloyd, as well as his work in the initial development of the experimental platform.

References

[1] S. A. Niknam, B. Davoodi, J. P. Davim, V. Songmene, Mechanical deburring and edge-finishing processes for aluminum parts–a review, The International Journal of Advanced Manufacturing Technology 95 (1) (2018) 1101–1125. doi:https://doi.org/10.1007/s00170-017-1288-8.

[2] K. Stouffer, R. Russell, R. Archacki, T. Engel, R. Dansereau, A. Grot, Advanced deburring and chamfering system (adacs) final report, National Institute of Standards and Technology (1996).

[3] Z. Roth, B. Mooring, B. Ravani, An overview of robot calibration, IEEE Journal on Robotics and Automation 3 (5) (1987) 377–385. doi:10.1109/JRA.1987.1087124.

[4] J. M. Hollerbach, C. W. Wampler, The Calibration Index and Taxonomy for Robot Kinematic Calibration Methods, The International Journal of Robotics Research 15 (6) (1996) 573–591. doi:10.1177/027836499601500604.

[5] M. R. Driels, W. Swayze, S. Potter, Full-pose calibration of a robot manipulator using a coordinate-measuring machine, The International Journal of Advanced Manufacturing Technology 8 (1) (1993) 34–41.

[6] A. Joubair, M. Slamani, I. A. Bonev, Kinematic calibration of a 3-dof planar parallel robot, Industrial Robot: An International Journal (2012). doi:https://doi.org/10.1108/01439911211227971.

[7] X. Zhang, Y. Song, Y. Yang, H. Pan, Stereo vision based autonomous robot calibration, Robotics and Autonomous Systems 93 (2017) 43–51. doi:https://doi.org/10.1016/j.robot.2017.04.001.

[8] A. Nubiola, M. Slamani, A. Joubair, I. A. Bonev, Comparison of two calibration methods for a small industrial robot based on an optical cmm and a laser tracker, Robotica 32 (3) (2014) 447. doi:https://doi.org/10.1017/S0263574713000714.

[9] A. Nubiola, I. A. Bonev, Absolute calibration of an ABB IRB 1600 robot using a laser tracker, Robotics and Computer-Integrated Manufacturing 29 (1) (2013) 236–245. doi:10.1016/j.rcim.2012.06.004.

[10] G. Luo, L. Zou, Z. Wang, C. Lv, J. Ou, Y. Huang, A novel kinematic parameters calibration method for industrial robot based on levenberg-marquardt and differential evolution hybrid algorithm, Robotics and Computer-Integrated Manufacturing 71 (2021) 102165. doi:https://doi.org/10.1016/j.rcim.2021.102165.

[11] L. Wu, H. Ren, Finding the kinematic base frame of a robot by hand-eye calibration using 3d position data, IEEE Transactions on Automation Science and Engineering 14 (1) (2017) 314–324. doi:10.1109/TASE.2016.2517674.

[12] S. He, L. Ma, C. Yan, C. H. Lee, P. Hu, Multiple location constraints based industrial robot kinematic parameter calibration and accuracy assessment, International Journal of Advanced Manufacturing Technology 102 (5-8) (2019) 1037–1050. doi:https://doi.org/10.1007/s00170-018-2948-z.

[13] Y. Guo, B. Song, X. Tang, X. Zhou, Z. Jiang, A measurement method for calibrating kinematic parameters of industrial robots with point constraint by a laser displacement sensor, Measurement Science and Technology 31 (7) (2020) 16. doi:10.1088/1361-6501/ab7bc1.

[14] C. Yu, J. Xi, Simultaneous and on-line calibration of a robot-based inspecting system, Robotics and Computer-Integrated Manufacturing 49 (2018) 349–360.

[15] R. Wang, A. Wu, X. Chen, J. Wang, A point and distance constraint based 6R robot calibration method through machine vision, Robotics and Computer-Integrated Manufacturing 65 (2020) 101959.

[16] S. Besnard, W. Khalil, G. Garcia, Geometric calibration of robots using multiple plane constraints, in: Advances in robot kinematics, Springer, 2000, pp. 61–70. doi:10.1007/978-94-011-4120-8_7.

[17] T. S. Lembono, F. Suárez-Ruiz, Q.-C. Pham, Scalar: Simultaneous calibration of 2-d laser and robot kinematic parameters using planarity and distance constraints, IEEE Transactions on Automation Science and Engineering 16 (4) (2019) 1971–1979. doi:https://doi.org/10.1109/TASE.2019.2918141.

[18] Y. J. Chiu, M. H. Perng, Self-calibration of a general hexapod manipulator using cylinder constraints, International Journal of Machine Tools and Manufacture 43 (10) (2003) 1051–1066. doi:10.1016/S0890-6955(03)00082-8.

[19] A. Joubair, I. A. Bonev, Kinematic calibration of a six-axis serial robot using distance and sphere constraints, The International Journal of Advanced Manufacturing Technology 77 (1-4) (2015) 515–523. doi:10.1007/s00170-014-6448-5.

[20] A. Goswami, A. Quaid, M. Peshkin, Complete parameter identification of a robot from partial pose information, in: [1993] Proceedings IEEE International Conference on Robotics and Automation, IEEE, 1993, pp. 168–173. doi:https://doi.org/10.1109/ROBOT.1993.291978.

[21] Z. Gan, Q. Tang, Calibration of a robot visual system, in: Visual Sensing and its Applications, Springer, 2011, pp. 93–141. doi:https://doi.org/10.1007/978-3-642-18287-7_4.

[22] Y. M. Zhao, Y. Lin, F. Xi, S. Guo, Calibration-based iterative learning control for path tracking of industrial robots, IEEE Transactions on industrial electronics 62 (5) (2014) 2921–2929. doi:https://doi.org/10.1109/TIE.2014.2364800.

[23] Y. Zeng, W. Tian, W. Liao, Positional error similarity analysis for error compensation of industrial robots, Robotics and Computer-Integrated Manufacturing 42 (2016) 113–120.

[24] Y. Guo, S. Yin, Y. Ren, J. Zhu, S. Yang, S. Ye, A multilevel calibration technique for an industrial robot with parallelogram mechanism, Precision Engineering 40 (2015) 261–272.

[25] L. Everett, Research topics in robot calibration, Robot Calibration (1993).

[26] S. Hayati, M. Mirmirani, Improving the absolute positioning accuracy of robot manipulators, Journal of Robotic Systems 2 (4) (1985) 397–413.

[27] R. Hartenberg, J. Danavit, Kinematic synthesis of linkages, New York: McGraw-Hill, 1964.

[28] L. J. Everett, T.-W. Hsu, The Theory of Kinematic Parameter Identification for Industrial Robots, Journal of Dynamic Systems, Measurement, and Control 110 (1) (1988) 96–100. doi:10.1115/1.3152658.

[29] G. Janez, K. Timi, G. Karl, B. Miran, Accuracy improvement of robotic machining based on robot's structural properties, International Journal of Advanced Manufacturing Technology 108 (5-6) (2020) 1309–1329.

[30] C.-C. Lu, Kinematic calibration of serial manipulators using relative measurements, Ph.D. thesis, Carleton University (2014).

[31] H. Zhuang, L. K. Wang, Z. S. Roth, Error-model-based robot calibration using a modified CPC model, Robotics and Computer Integrated Manufacturing 10 (4) (1993) 287–299.

[32] J. Y. Luh, R. P. Paul, M. W. Walker, Resolved-Acceleration Control of Mechanical Manipulators, IEEE Transactions on Automatic Control 25 (3) (1980) 468–474. doi:10.1109/TAC.1980.1102367.

[33] Northern Digital Inc., Optotrak Certus Technical Specifications (2015).